remote sensing

MDPI

Article

Evaluation of Boundary Layer Characteristics at Mount Si'e Based on UAV and Lidar Data

Jiantao Dang [1], Xinrui Xie [2] and Xiaohang Wen [2,*]

[1] The Technical Department of Xichang Satellite, Xichang 615000, China; jiantao_dang@163.com
[2] Plateau Atmosphere and Environment Key Laboratory of Sichuan Province, College of Atmospheric Sciences, Chengdu University of Information Technology, Chengdu 610225, China; 3230101090@stu.cuit.edu.cn
* Correspondence: wxh@cuit.edu.cn

Abstract: The atmospheric boundary layer is a crucial transitional region connecting the surface with the free atmosphere, playing a bridging role in land-sea-air interactions and the interactions between different atmospheric layers. This study utilizes rotary-wing UAVs, high-resolution lidar, and WRF simulation data to analyze the vertical distribution characteristics of temperature, humidity, wind speed, and wind direction boundary layer over the Mount Si'e region in 4–6 April 2024. The results indicate that the boundary layer temperature decreases with increasing altitude, reaching up to 18°C, while humidity decreases with height, dropping to as low as 35%. Daytime wind speeds range from 4 to 8 m/s, decreasing to 2 to 4 m/s at night. The boundary layer height can reach up to 900 m during the day and drops to 100–200 m at night, showing distinct diurnal variation characteristics. UAV observations are in good agreement with lidar and WRF simulation results, highlighting the application value of UAVs in high temporal and spatial resolution boundary layer studies. The study also reveals the significant impact of complex terrain on boundary layer characteristics, providing scientific insights into the dynamic and thermal processes of the boundary layer and offering reference value for improving regional weather forecasting and numerical simulations.

Keywords: atmospheric boundary layer; LiDAR; UAV; wind profile; ABLH

check for updates

Citation: Dang, J.; Xie, X.; Wen, X. Evaluation of Boundary Layer Characteristics at Mount Si'e Based on UAV and Lidar Data. *Remote Sens.* **2024**, *16*, 3816. https://doi.org/10.3390/rs16203816

Academic Editors: Tamas Várnai, Massimo Menenti, Yaoming Ma, Li Jia and Lei Zhong

Received: 29 August 2024
Revised: 9 October 2024
Accepted: 10 October 2024
Published: 14 October 2024

Copyright: © 2024 by the authors. Licensee MDPI, Basel, Switzerland. This article is an open access article distributed under the terms and conditions of the Creative Commons Attribution (CC BY) license (https://creativecommons.org/licenses/by/4.0/).

1. Introduction

The atmospheric boundary layer (ABL), also known as the planetary boundary layer, is the transitional zone between the surface-disturbed airflow and the free atmosphere where friction is negligible [1]. It is directly influenced by surface conditions and responds to these effects within an hour or less, with its height reaching up to several kilometers. It serves as a vital channel for the transport of momentum, heat, and various substances within the Earth's atmosphere, playing a significant role in the exchange of energy and matter between the Earth's surface and the free atmosphere [2–4]. A deeper understanding of the structure and characteristics of the boundary layer will help improve our understanding of energy and matter transfer and cycling within the Earth system [4–7]. The average elevation of the plateau exceeds 4 km, and it features a unique atmospheric boundary layer formed by intense solar radiation, resulting in significant temperature differences between the surface and the complex terrain [7,8]. The interaction between the intricate topography of the eastern plateau and diverse circulation systems creates the region's unique weather and climate characteristics. Therefore, studying the atmospheric boundary layer structure in this area is crucial for understanding the causes of weather and climate and their impacts on China's weather [9,10].

The atmospheric boundary layer (ABL) on the Tibetan Plateau has been a focal point of research due to its significant scientific value. Over the past decades, numerous studies have explored the ABL height (ABLH) and the vertical distribution of meteorological elements within the boundary layer across the plateau. The ABLH generally ranges from 2000 to 5000 m, with substantial regional and seasonal variations. For example, Duzheng Ye [11]

reported an ABLH between 2000 and 3000 m, while other studies observed variations across different regions, such as around 2250 m in Dangxiong County [12], up to 3880 m in the Everest region [13], and as high as 5000 m in Gaize [14]. In northern areas of the plateau, such as Anduo and Naqu, the convective boundary layer can extend to around 3200 m, whereas the stable boundary layer typically remains much lower, around 1000 m [15].

The ABLH also exhibits significant diurnal and seasonal variations throughout the plateau. It generally increases rapidly from sunrise to noon, stabilizes in the afternoon, and decreases significantly at night [16,17]. During summer, the convective boundary layer can reach up to 4000 m, while the stable boundary layer dominates in the morning hours [18]. Seasonal variations show that the ABLH tends to be higher in spring and summer, especially in the eastern and western regions of the plateau, while it drops significantly during winter and rainy seasons in central and northern areas [19,20].

In summary, the ABLH generally peaks in the eastern plateau during spring, in the western plateau during summer, and in the central plateau during spring and autumn, with lower values observed during winter across most regions. Studies using COSMIC data have shown that, on average, the ABLH in winter exceeds 2000 m, decreases slightly in spring, rises again in summer, and drops in autumn [21]. Over the past 30 years, the ABLH on the plateau has shown a general increasing trend in winter, particularly since the early 21st century [22]. These variations in ABLH reflect the complex interplay between topography, weather systems, and surface conditions on the Tibetan Plateau, underscoring the need for high-resolution studies to better capture these dynamics.

Mount Si'e is located on the southeastern edge of the Tibetan Plateau, at the transition zone between the main body of the Tibetan Plateau and the Sichuan Basin. Although many studies have analyzed the variations of near-surface meteorological elements on the Tibetan Plateau, research on the eastern edge of the plateau remains limited, despite its significant impact on regional weather and climate patterns [23]. Moreover, existing studies on the atmospheric boundary layer (ABL) of the Tibetan Plateau are often constrained by low spatial and temporal resolution, which can result in certain limitations, such as an inability to capture fine-scale boundary layer processes and potential inaccuracies in representing local meteorological phenomena.

This study compares and analyzes UAV observations and WRF simulation data from 4–6 April 2024, at the Mount Si'e station on the southeastern edge of the plateau. Combined with lidar data from the Mount Si'e station, the study investigates the boundary layer characteristics in the eastern part of the plateau. The use of high-resolution UAV and lidar data allows for a detailed examination of the fine-scale boundary layer processes that were previously difficult to capture with conventional methods. By addressing the limitations of low spatial and temporal resolution found in earlier studies, this research aims to provide a more accurate and comprehensive understanding of the boundary layer structure and dynamics in this region. These advanced observational techniques help correct potential inaccuracies in previous findings and offer valuable insights for studying weather development and climate change in complex terrains like the southeastern Tibetan Plateau.

2. Materials and Methods

2.1. Data

The study area is located on Mount Si'e, where the atmospheric observations are conducted. Figure 1 illustrates the topography and vegetation fraction of the study area, providing context for the following sections.

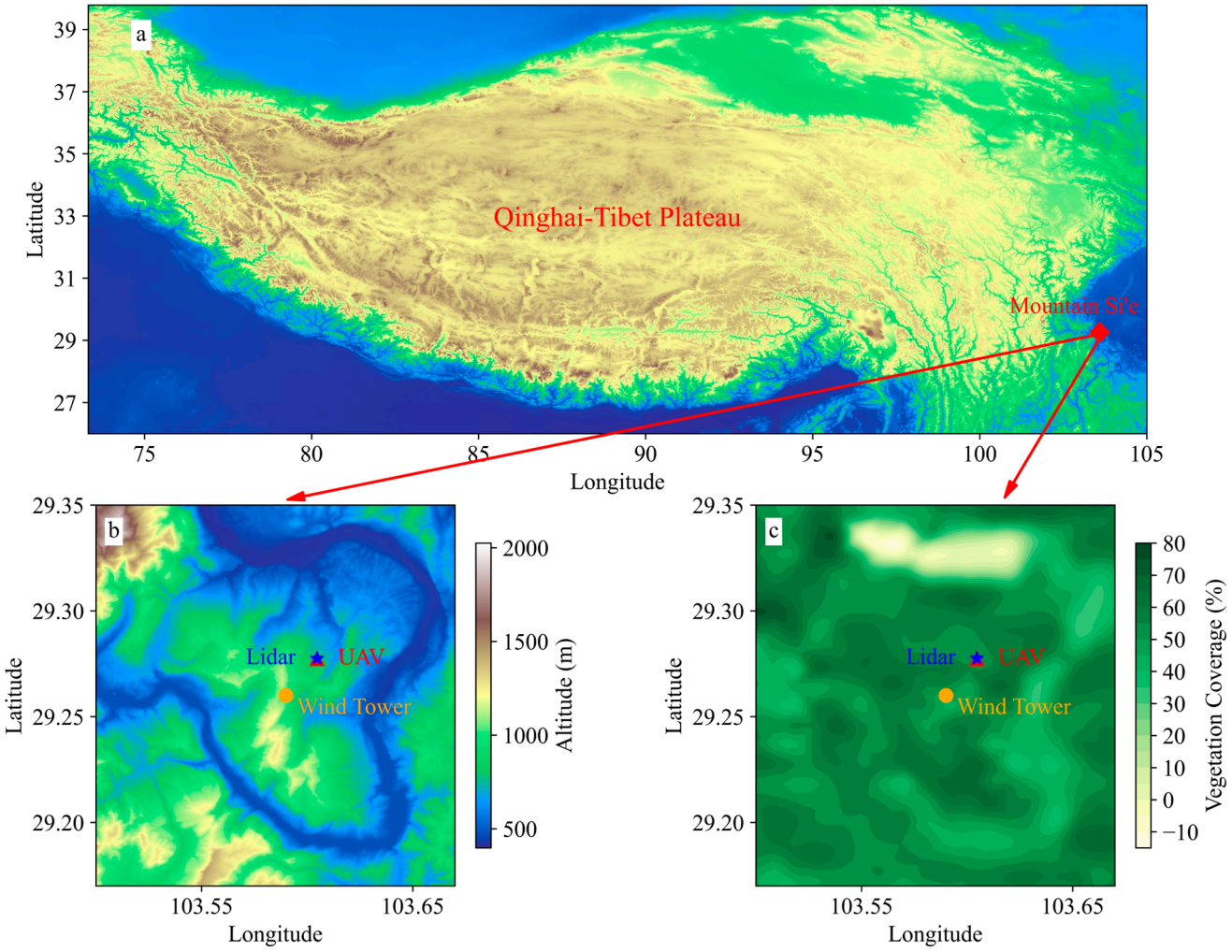


Figure 1. (**a**,**b**) The topography of Mount Si'e; (**c**) The vegetation fraction of Mount Si'e.

2.1.1. UAV Observation Data

The Unmanned Aerial Vehicle (UAV) observation data used in this study are derived from the Rotary Wing UAV Boundary Layer Meteorological Integrated Detection System (RWBMIS) by DJI Innovations M300 RTK Model, China. In this system, a rotary-wing UAV is used as a carrier to carry the Spirit Sniff Mini2 monitoring module, manufactured by Shenzhen Kefei Technology Co., Ltd., Shenzhen, China, to complete the observation of temperature, pressure, humidity, wind and other meteorological elements contours in a mobile observation mode. The UAV performs vertical ascents and descents during high-altitude detection experiments, with an ascent speed of 2 m/s. It offers a time resolution of 1 s and a vertical resolution of 1 m. The sensor is based on the ultrasonic measurement method without moving parts, with UAV translational motion compensation algorithm, UAV attitude compensation algorithm, and UAV rotational motion compensation algorithm, which can realize the measurement of real wind speed and direction information while moving, with fast response rate, small systematic error and high accuracy (Figure 2b). Due to the obvious time lag in the downlink data of the UAV, only 2 m/s uplink data is used in this study.

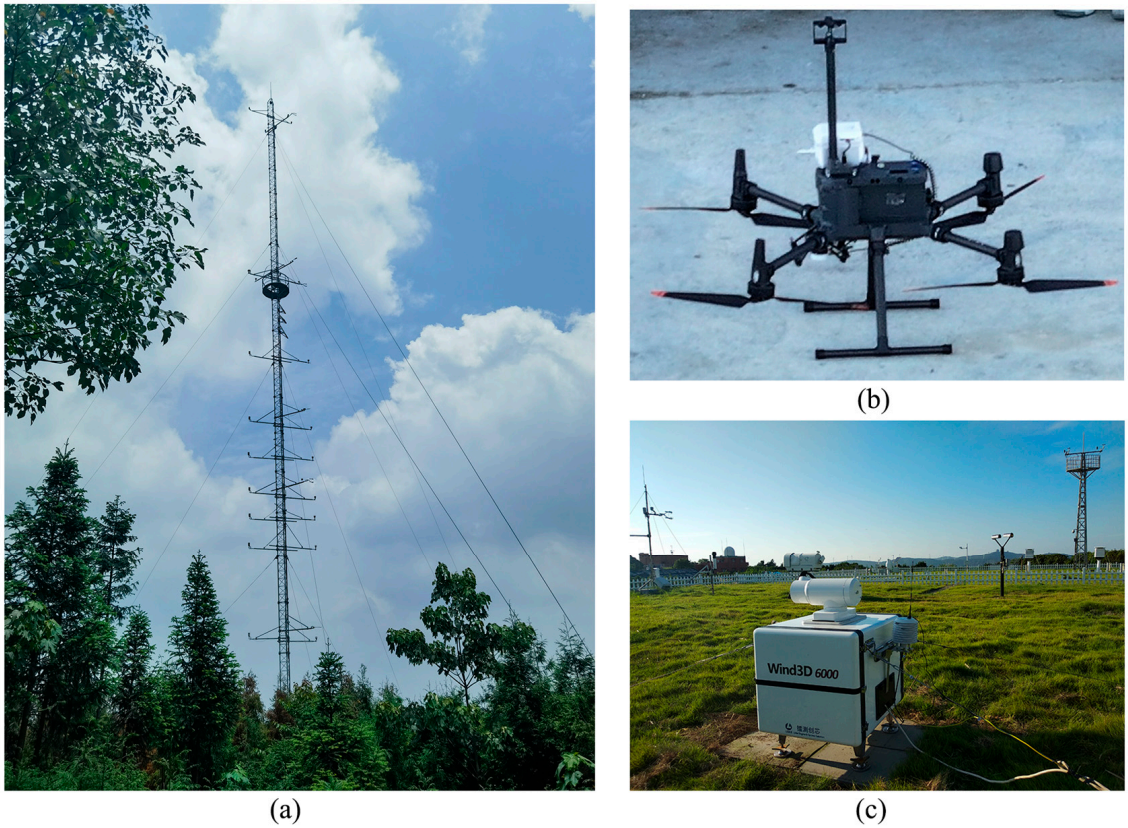


Figure 2. (**a**) Wind Tower at Mount Si'e; (**b**) UVA; (**c**) Lidar Wind3D 6000.

Table 1 lists the basic performance param of the rotary-wing UAV used in this study in detail.

Table 1. Measurement Param of UAV Meteorological Observation Systems.

Measuring Element	Measuring Range	Resolution	Accuracy
Temperature	−40~+80 °C	0.1 °C	±0.1 °C (+15~+25 °C); ±0.15 °C (0~+15 °C, +25~+40 °C); ±0.4 °C (−40~0 °C, +40~+80 °C)
Pressure	300~1100 hPa	0.1 hPa	±0.1 °C (+15~+25 °C); ±0.15 °C (0~+15 °C, +25~+40 °C); ±0.4 °C (−40~0 °C, +40~+80 °C)
Humidity	0~100% RH	0.1% RH	0~+40 °C: ±1.5% RH (0~90% RH); ±2.5% RH (90~100% RH) −40~0 °C, +40~+80 °C: ±3.0% RH (0~90% RH); ±4.0% RH (90~100% RH)
Wind Speed	0~50 m/s	0.1 m/s	±0.1 m/s (0–10 m/s); ±1% (11–30 m/s); ±2% (31–50 m/s)
Wind Direction	0~365°	±0.1°	1°

2.1.2. LiDAR Data

The wind speed and wind direction data used in this study were obtained from the Wind3D 6000, a three-dimensional scanning wind lidar manufactured by Qingdao Leice Transient Technology Co., Ltd., Qingdao, China (Figure 2c). Lidar (Light Detection and Ranging) operates on the principle of optical pulse coherent Doppler frequency shift detection, enabling fine-scale detection of three-dimensional wind fields in the lower and middle troposphere, including the atmospheric boundary layer. The Wind3D 6000 is equipped with a high-precision optical scanning mirror, supporting various three-dimensional scanning modes, such as Doppler Beam Swinging (DBS), Velocity Azimuth Display (VAD), Plan Position Indicator (PPI), Range Height Indicator (RHI), and Constant Altitude Plan Position Indicator (CAPPI). The maximum detection radius can reach up to 6 km, covering all the

requirements of the study area. In this study, only data below 1500 m were used to facilitate comparative analysis with observational data. Table 2 details the basic performance param of the Wind3D 6000 lidar system used in this research.

Table 2. Technical Specifications of the Wind3D 6000 Lidar.

Indicator	Parameter
Operating Wavelength	1.5 μm
Detection Range	45–6000 m
Spatial Distance Resolution	45–6000 m
Temporal Resolution	4.5–150 m
Horizontal Wind Speed Measurement Error	Wind Speed Line ≤ 1 m/s
Horizontal Wind Direction Measurement Error	≤3°
Scanning Angle Accuracy	≤0.1°
Scanning Modes	Plan Position Indicator (PPI), Range Height Indicator (RHI), Doppler Beam Swinging (DBS), Sector Scanning, Volume Scanning, Custom Scanning Modes

2.1.3. Wind Tower Data

The wind speed and wind direction data used in this study, recorded at 1-min intervals over two days from 4–6 April 2024, were obtained from the Emei Mountain Atmospheric and Environmental Comprehensive Observation and Experiment Station of Chengdu University of Information Technology. This station (Figure 1a) is located on Mountain Si'e (29.26°N, 103.59°E) at an altitude of 970 m and will hereafter be referred to as the Mount Si'e Station. The Mount Si'e Station is situated in Mount Si'e Village, Hulu Ba Town, Shawan District, Leshan, Sichuan Province, southeast of the main peak of Mount Emei, Jin Ding, and 37.4 km away from it. Apart from higher elevation mountains to the northwest, the station is surrounded by the Dadu River on all other sides. The underlying surface is a complex mountainous forest with an average forest canopy height of 14 m. Mount Si'e falls within the subtropical montane evergreen broad-leaved forest climate zone, characterized by warm winters, hot summers, and abundant rainfall.

The meteorological gradient observation tower at the station is 60 m high and is equipped with an eddy covariance observation system, including a Campbell CSAT3A 3D ultrasonic anemometer, EC150 infrared CO_2 and H_2O gas analyzers, and a CNR-1 four-component radiometer (Figure 2a). There are five observation levels for wind speed, wind direction, air temperature, and relative humidity: two levels within the canopy at 2 m and 10 m, and three levels above the canopy at 20 m, 25 m, and 58 m. Rain gauges are installed at 38 m and 2 m to measure precipitation and canopy-intercepted rainfall. The flux observation system's ultrasonic probes are installed at 38 m. Data collection is performed using the Campbell CR6 Series data logger, with the eddy covariance system operating at a sampling frequency of 10 Hz.

2.2. WRF Simulation Design

The WRF is a next-generation mesoscale forecast model with a data-assimilation system that advances both the understanding and prediction of mesoscale weather and accelerates the transfer of research advances into operations. It was developed collaboratively by NCAR and the National Centers for Environmental Prediction (NCEP; http://www.mmm.ucar.edu/wrf/users/, accessed on 12 April 2024). The WRF version 3.7.1 modeling system, released in August 2015, is used in this study. The domain configuration features a 25-km resolution single grid system with the center located at 103.59°E, 29.26°N. The simulated area ranges from 70.47°E to 135.53°E longitude and 18.28°N to 53.57°N latitude, with a temporal resolution of 3 h.

Initial and boundary conditions for the large-scale atmospheric fields, as well as initial soil param (soil water, moisture, and temperature), are given by the 1° × 1° NCEP Global Final Analysis (FNL). The use of the FNL provides an upper bound on the skill

that is achievable with regional climate prediction models. Boundary conditions at the specified zone are determined entirely by temporal interpolation from the 6-hourly FNL data [24]. Since the domain boundaries are located at the edge of the Tibet Plateau, there are high mountain areas with big topographic relief. In order to avoid vertical interpolation problems caused by the differences in topography between the forcing data in WRF model, 35 unevenly spaced full Eta levels were defined in the vertical dimension (eta level = 1.000, 0.995, 0.983, 0.970, 0.954, 0.934, 0.909, 0.880, 0.845, 0.807, 0.520, 0.468, 0.420, 0.376, 0.335, 0.298, 0.263, 0.231, 0.202, 0.175, 0.150, 0.127, 0.106, 0.088, 0.070, 0.055, 0.040, 0.026, 0.013, 0.000). The vertical coordinate η is defined as:

$$\eta = \frac{p_h - p_{ht}}{p_{hs} - p_{ht}} \tag{1}$$

where p_h is the hydrostatic component of the pressure, p_{hs} is surface pressure, and p_{ht} is a constant pressure at the model top (50 hPa) from the surface are used [24].

The details of the physical parameterizations are summarized in Table 3.

Table 3. Summary of the WRF configuration.

Physical Parameterizations	Configuration
Microphysics	Lin scheme
Cumulus parameterization	Tiedtke scheme
Longwave radiation	RRTM scheme
Shortwave radiation	Dudhia scheme
Cumulus clouds	Kain-Fritsch convection scheme
Planetary boundary layer	YSU PBL scheme
Surface layer	Noah land surface model

2.3. Calculation Method of ABLH

To facilitate analysis and comparison, this study divides the boundary layer into the convective boundary layer (CBL) and the stable boundary layer (SBL) for analysis. This classification is based on the potential temperature profile and the Richardson number (*Ri*). The boundary layer height is estimated using the parcel method and the Ri method, respectively. The calculation formula for *Ri* is as follows [25]:

$$Ri(z) = \frac{g(z - z_0)}{\theta_v(z)} \frac{\theta_v(z) - \theta_v(z_0)}{u(z)^2 + v(z)^2} \tag{2}$$

$$u(z) = V(z) \sin \alpha(z) \tag{3}$$

$$v(z) = V(z) cos\alpha(z) \tag{4}$$

where g is the acceleration due to gravity (9.81 m/s^2), z_0 is the ground elevation, θ_v is the imaginary temperature, u and v are the zonal and meridional wind components, respectively, V is the wind speed, and α is the wind direction.

The calculation of the imaginary temperature (θ_v) is as follows:

$$r_s = \frac{\varepsilon e_s}{P} \tag{5}$$

$$\begin{cases} t \geq 0, e_s = 6.112 e^{\left(\frac{17.67t}{t+243.5}\right)} \\ t < 0, e_s = 6.1078 \times 10^{\left(\frac{7.5t}{t+237.3}\right)} \end{cases} \tag{6}$$

$$U_w = \frac{r_s}{r} \tag{7}$$

$$\theta_v = \theta(1 + 0.608r) \tag{8}$$

where r_s is the saturation mixing ratio, with $\varepsilon \approx 0.622$, r is the mixing ratio, e_s is the saturation vapor pressure, t is the temperature in degrees Celsius, U_w is the relative humidity, P is the atmospheric pressure, θ is the potential temperature.

The diagnostic methods for boundary layer height are as follows [26]:

$$\begin{cases} \theta_{200} - \theta_0 < 0, R_i(0 \sim 100) < 0 & \text{CBL} \\ else & \text{SBL} \end{cases} \quad (9)$$

here, θ_{200} and θ_0 represent the potential temperature at 200 m and at the surface.

The parcel method defines the boundary layer height as the altitude where a parcel of air, with an initial virtual potential temperature (θ_{v0}) equal to the maximum at the surface, reaches the same virtual potential temperature again upon vertical ascent. This method is used when the atmospheric boundary layer (ABL) is a convective boundary layer (CBL). When the ABL is a stable boundary layer (SBL), the *Ri* method is typically used to estimate the boundary layer height. The height of the SBL is defined as the level where the Richardson number equals or exceeds a specified critical value. In this study, the critical Richardson number (*Ric*) is set to *Ric* = 0.25.

3. Results

3.1. Vertical Variation Characteristics of Meteorological Elements in ABL

3.1.1. Vertical Profiles of Temperature, Pressure, and Humidity

Figure 3 illustrates the vertical distribution characteristics of temperature, pressure, and humidity at different times as observed by UAV soundings over the Mount Si'e Station. From the figure, it can be observed that temperature, pressure, and humidity exhibit regular variations, generally showing a decreasing trend with increasing altitude. Figure 1 also reveals distinct diurnal variation patterns: during the day, temperatures rise, humidity decreases, and pressure remains stable; at night, temperatures fall, humidity increases and pressure changes are minimal.

During the daytime (4 April at 16:00 and 17:00; CST, the same below), surface temperatures are relatively high, with a rapid decrease in temperature near the surface. The temperature is around 18°C near the ground and gradually decreases to about 8 °C with increasing altitude. This indicates that solar radiation during the day significantly increases the surface temperature, creating a pronounced temperature gradient. At night (4 April at 23:00 and 5 April at 09:00), temperatures are generally lower, especially near the surface, where the temperature gradient is smaller, indicating a relatively uniform temperature profile. This may be due to nighttime radiative cooling at the surface, significantly lowering the near-surface temperature and increasing the stability of the ABL, thereby suppressing vertical heat mixing. In the morning (5 April at 10:00 and 6 April at 09:00), solar radiation gradually intensifies, leading to a rise in temperature (Figure 3).

Pressure variations with height are minimal, and the pressure curves at different times nearly overlap, indicating that the vertical distribution of pressure is relatively stable during these observation periods. This stability in pressure suggests that no significant weather systems were interfering during the observations, and the pressure field remained relatively consistent over these periods.

The lowest humidity during the daytime is observed at 14:00 on 5 April, with minimum humidity reaching about 35%. This indicates that enhanced solar radiation during the day intensifies the evaporation at the surface and in the lower atmosphere, making the air drier [1]. At night, humidity is higher, particularly near the surface, exceeding 50%. This phenomenon can be explained by the drop in temperature at night, causing water vapor in the air to condense more easily, thereby increasing near-surface humidity [27,28]. Additionally, humidity is higher in the lower layers (from the surface to around 200 m) and decreases rapidly with height, which may be related to variations in atmospheric mixing processes and turbulence activity [29].

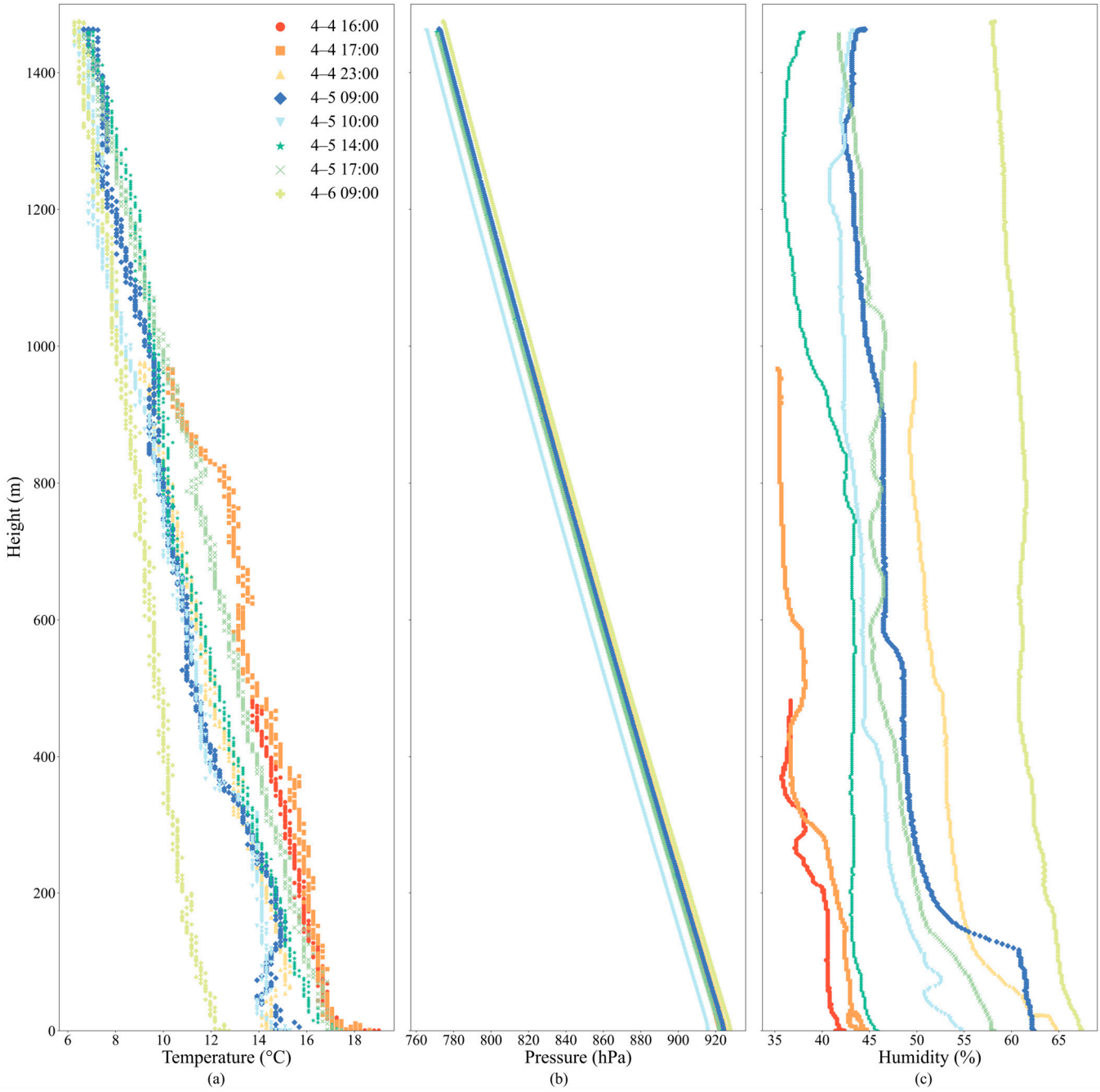


Figure 3. Vertical Distribution of (**a**) Temperature, (**b**) Pressure, and (**c**) Humidity Observed by UAV at Different Times.

3.1.2. Vertical Variation Characteristics of Wind Speed and Wind Direction

Figure 1b,c show the topography and vegetation fraction of the Mount Si'e region. The complex mountainous terrain and dense forest cover significantly impact the local wind field, creating a unique pattern of wind speed and direction distribution. Figure 4 shows that the main wind directions during April at the Mount Si'e area are concentrated in the south-southwest (SSW), south (S), and southwest (SW) directions. These directions not only exhibit a higher frequency of occurrence but also have relatively strong wind speeds. Particularly in the southwest and south-southwest directions, wind speeds often range between 4–8 m/s and sometimes even exceed 8 m/s. The figure also indicates a noticeable presence of northerly (N) winds. Although less frequent than the south-southwest and southwest winds, the northerly winds still have some influence. The wind speeds of

the northerly winds are mostly in the low to moderate range (0–4 m/s), indicating that while northerly winds occur during April, their intensity is relatively weak. Overall, the April wind field characteristics at Mount Si'e are distinct, with a clear dominance of south-southwest and southwest winds, which are accompanied by higher wind speeds, whereas the occurrence of northerly winds is relatively infrequent and less intense.

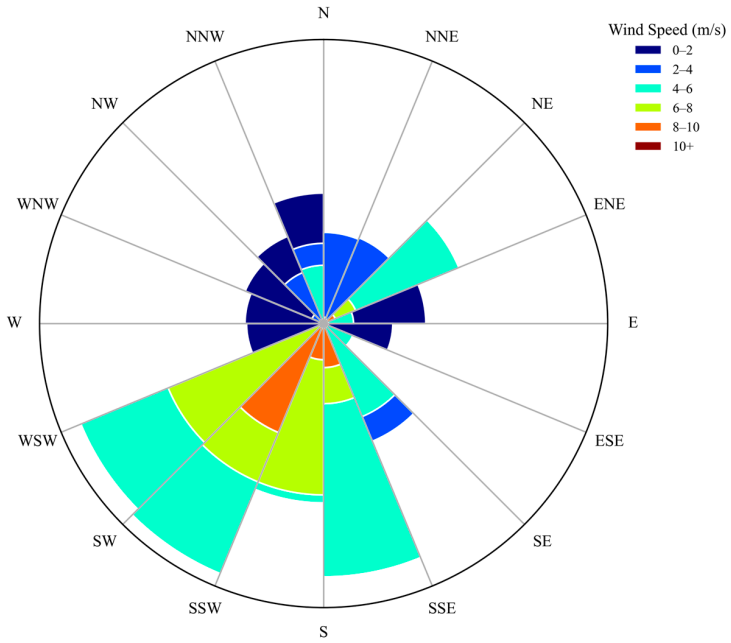


Figure 4. Wind rose diagram based on cumulative UAV observation data over the study period.

These wind direction and wind speed distribution characteristics are closely related to the complex mountainous forest's terrain of the Mount Si'e region. Complex mountainous terrain and forest cover typically significantly alter the local wind speed and direction distribution. The variations in elevation and vegetation density create wind corridors that channel the winds in specific directions, particularly from the southwest and south-southwest, enhancing wind speeds in these directions. The higher wind speeds in the south-southwest and southwest directions may be associated with the wind corridor effect created by the terrain undulations and variations in forest density in these directions, where the guidance of the terrain enhances the wind speed. The presence of forest vegetation can increase surface roughness, thereby reducing low-level wind speeds. However, in a complex mountainous environment, the interaction between terrain and vegetation can create zones of enhanced wind speed. In regions with dense forest cover, wind speeds tend to be lower near the ground due to increased surface roughness, while in open areas or along wind corridors, wind speeds can increase significantly. Changes in wind speed are also related to the microclimatic effects of the forest. Forest cover can alter thermal conditions at the surface, influencing vertical air movement and wind speed distribution. Forests can release moisture through transpiration, creating localized moist air regions near the ground. These areas tend to have relatively lower wind speeds, while higher wind speeds may occur in more open areas.

The influence of the mountainous terrain is also evident in the vertical distribution of wind characteristics, as shown in Figure 5. Figure 5, showing wind rose diagrams at different altitude levels, further reveals the vertical distribution characteristics of wind speed and direction. In the lower layer (0–200 m), wind speeds are primarily concentrated between 0–2 m/s and 2–4 m/s, with more dispersed wind directions. This aligns with the complex mountainous forest environment at the surface, where the forest canopy increases surface friction and local terrain induces changes in wind direction. As altitude increases, the influence of surface features diminishes, and wind directions become more aligned with larger-scale atmospheric flows. At the 200–600 m altitude layer, wind speeds increase,

mainly ranging between 2–4 m/s and 4–6 m/s, and wind directions become more focused, showing enhancement from the southwest and southeast directions. This suggests that as altitude increases, the influence of terrain on the wind field gradually diminishes, and the impact of larger-scale weather systems becomes more apparent. At even higher altitudes, in the 600–1000 m and 1000–1500 m layers, wind speeds increase significantly, concentrating between 4–6 m/s and 8–10 m/s, with wind directions mainly from the south. This indicates more pronounced characteristics of large-scale atmospheric circulation, with the direct influence of the mountainous forest underlying surface substantially reduced.

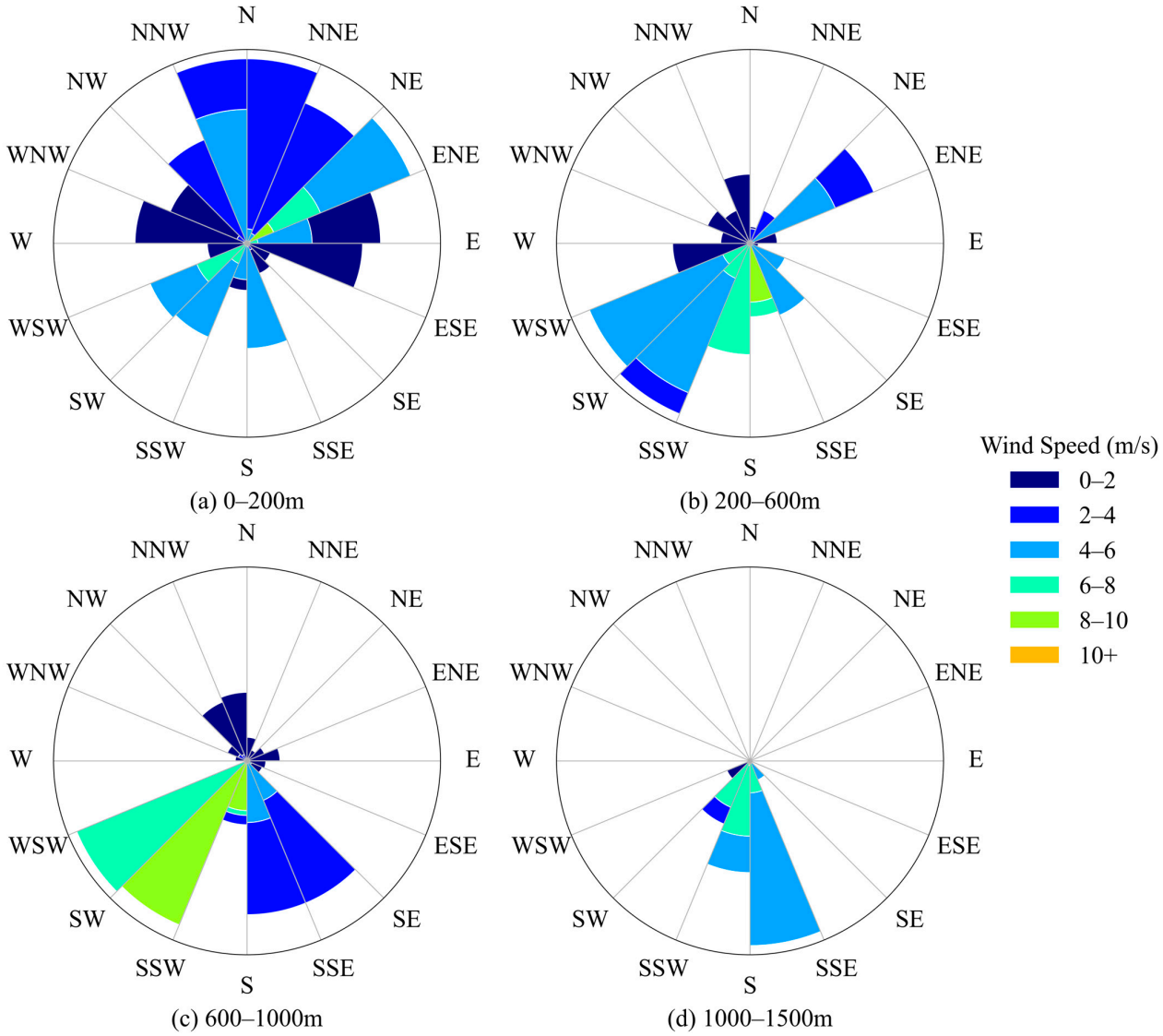


Figure 5. Wind Rose Diagrams at Different Altitude Levels (based on cumulative UAV observation data over the study period).

These changes in wind speed and direction are closely related to the presence of large-scale weather systems, such as troughs of low pressure or ridges of high pressure, and the diurnal variation processes induced by surface heating and cooling. The development of the atmospheric boundary layer increases in thickness due to surface heating during the day, enhancing turbulence and enabling the upward transfer of momentum, resulting in a significant increase in wind speed at higher levels. At night or in the early morning, surface cooling causes the boundary layer to thin, leading to a reduction in wind speed. Moreover, convective diffusion processes also transfer momentum vertically from lower to higher levels, which is particularly evident during the day.

In summary, the complex mountainous forest underlying surface conditions result in lower wind speeds and more dispersed wind directions at lower levels. In contrast, at higher levels, large-scale atmospheric circulation begins to dominate, leading to increased wind speeds and more concentrated wind directions. This vertical variation pattern is a result of the interaction between atmospheric dynamic and thermal processes, particularly under the influence of atmospheric boundary layer development and convective diffusion.

Figure 4 presents the vertical profiles of boundary layer wind speed at different times over the Mount Si'e region from 4–5 April 2024. The wind speed distribution varies at different times. Overall, at lower altitudes (typically below 400 m), the wind speed fluctuates more significantly, while with increasing altitude, the wind speed tends to stabilize, and the profiles become smoother above 600 m. The wind speed profiles also show distinct diurnal variation characteristics. During the day (Figure 6f,g), wind speeds are relatively high between the surface and 400 m, ranging from 4–6 m/s, and at higher altitudes (Figure 6f), they can reach close to 8 m/s. This phenomenon is related to the enhancement of thermal turbulence caused by solar radiation heating the surface during the day, leading to increased wind speeds in the lower layers. At night (Figure 6c,e), the lower layer wind speeds are lower, usually around 2–4 m/s, and calm regions with near-zero wind speed appear at some altitudes. This could be due to the presence of an inversion layer or the formation of a stable boundary layer structure, which weakens turbulence and reduces wind speed.

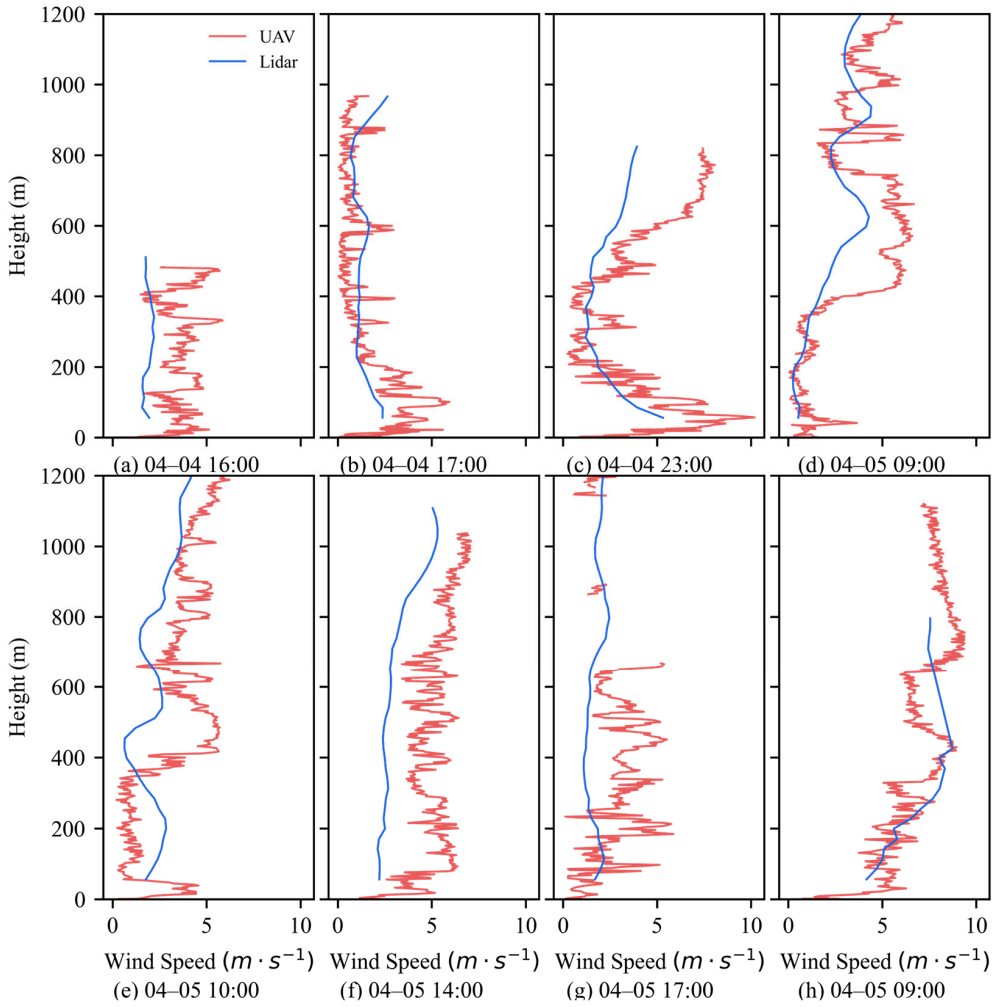


Figure 6. Comparison of April Boundary Layer Wind Speed Vertical Profiles at Mount Si'e.

The diurnal variation in wind speed may be influenced by changes in the local pressure gradient, terrain effects, and temperature differences between day and night [30]. During

the day, solar radiation heats the surface, enhancing turbulence mixing in the boundary layer and leading to increased wind speeds [31]. At night, surface cooling due to heat loss stabilizes the boundary layer, suppressing turbulence and reducing wind speeds. The variations in the strength of turbulent diffusion also contribute to the day-night differences in wind speed distribution. During the day, strong turbulence results in more uniform wind speed distribution, while at night, reduced turbulence increases the wind speed gradient, creating noticeable vertical differences in wind speed distribution.

The trends observed from UAV and lidar data are generally similar, showing strong consistency in wind speed variations at larger scales. However, UAV observations provide higher-resolution wind speed data, revealing more detailed fluctuations, which is a significant advantage over lidar data.

Figure 7 shows the vertical profiles of wind direction at different times in the Mount Si'e region. The figure indicates significant changes in wind direction at different times and altitude levels. At 16:00 on 4 April, the wind direction gradually shifts from southerly near the surface to southwesterly at higher altitudes, possibly related to thermal differences induced by daytime solar radiation, which promote changes in the local wind field. At 17:00, there are significant fluctuations in wind direction across different altitude levels, with southerly winds in the lower layers and easterly winds in the higher layers, suggesting the possible presence of an inversion layer or turbulence activities within the boundary layer causing vertical differences in wind direction. At 23:00, the wind direction is easterly in the lower layers and southerly in the higher layers, indicating characteristics associated with the formation of a stable stratification at night.

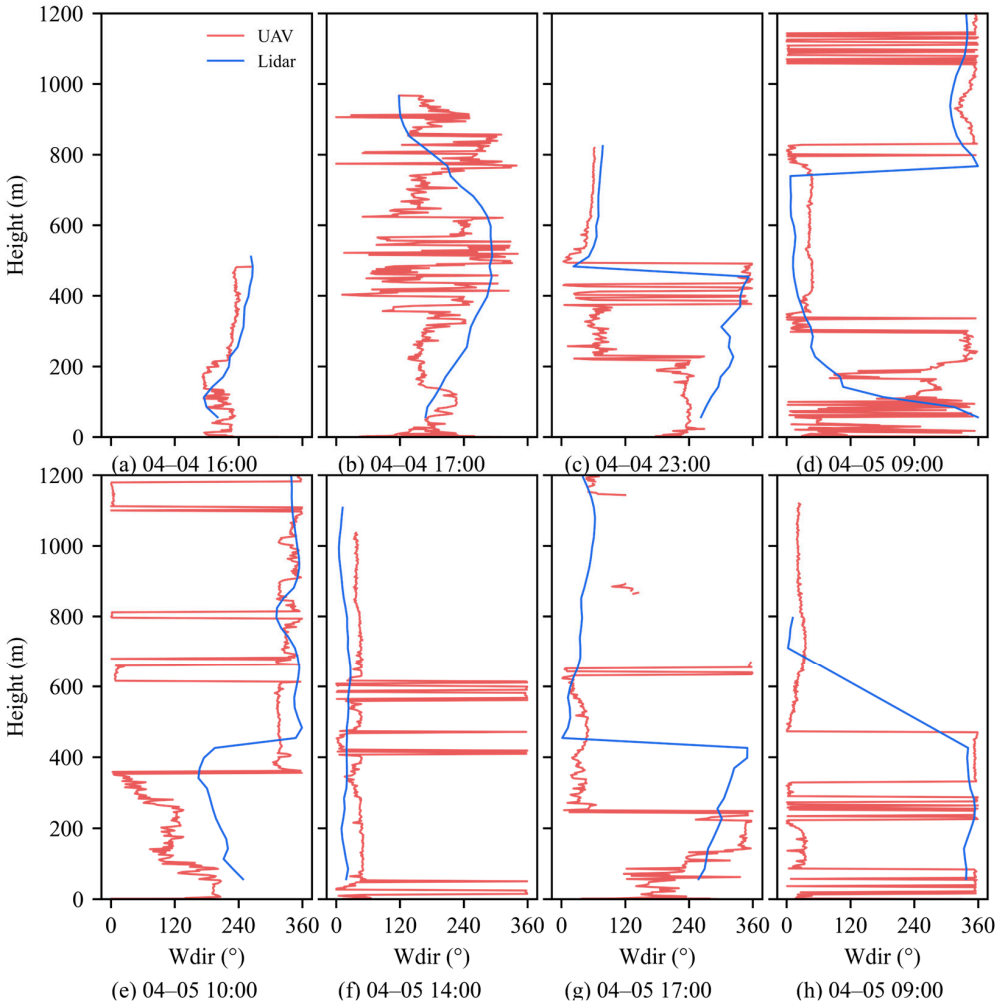


Figure 7. Comparison of April Boundary Layer Wind Direction Vertical Profiles at Mount Si'e.

In the morning of 5 April (09:00 and 10:00), the lower layer wind direction is northerly and northwesterly, gradually shifting to southerly and southwesterly in the mid-upper layers. This transition in wind direction may be related to the dissipation of the nocturnal radiative inversion layer and the redevelopment of the boundary layer in the morning. At 14:00, there is a significant change in wind direction, with easterly winds in the lower layers and southerly winds in the higher layers, possibly due to local thermal and momentum exchange processes. At 17:00, the wind direction in the lower layers is southerly, gradually shifting to easterly at higher altitudes, indicating that during the afternoon development of the boundary layer, wind direction is significantly influenced by turbulence mixing. At 09:00 on 5 April, the wind direction again transitions from northerly near the surface to southwesterly in the mid-upper layers, consistent with the characteristics of the developing boundary layer in the morning.

The trends observed from UAV and lidar data remain largely consistent, showing strong agreement. However, UAV observations can capture more detailed fluctuations in wind direction, demonstrating an advantage over lidar observations.

Figure 8 shows the temporal variation of wind speed and wind direction in the low levels of the boundary layer over the Mount Si'e region. The figure reveals distinct diurnal variation characteristics in both wind speed and wind direction. During the daytime, especially at higher levels (38 m and 58 m), wind speed significantly increases, reaching its maximum. This could be attributed to enhanced atmospheric turbulence caused by increased solar radiation during the day, which raises wind speeds. In contrast, wind speeds decrease significantly at night, particularly at lower levels (2 m and 10 m), a phenomenon that may be associated with stable stratification due to nighttime surface cooling.

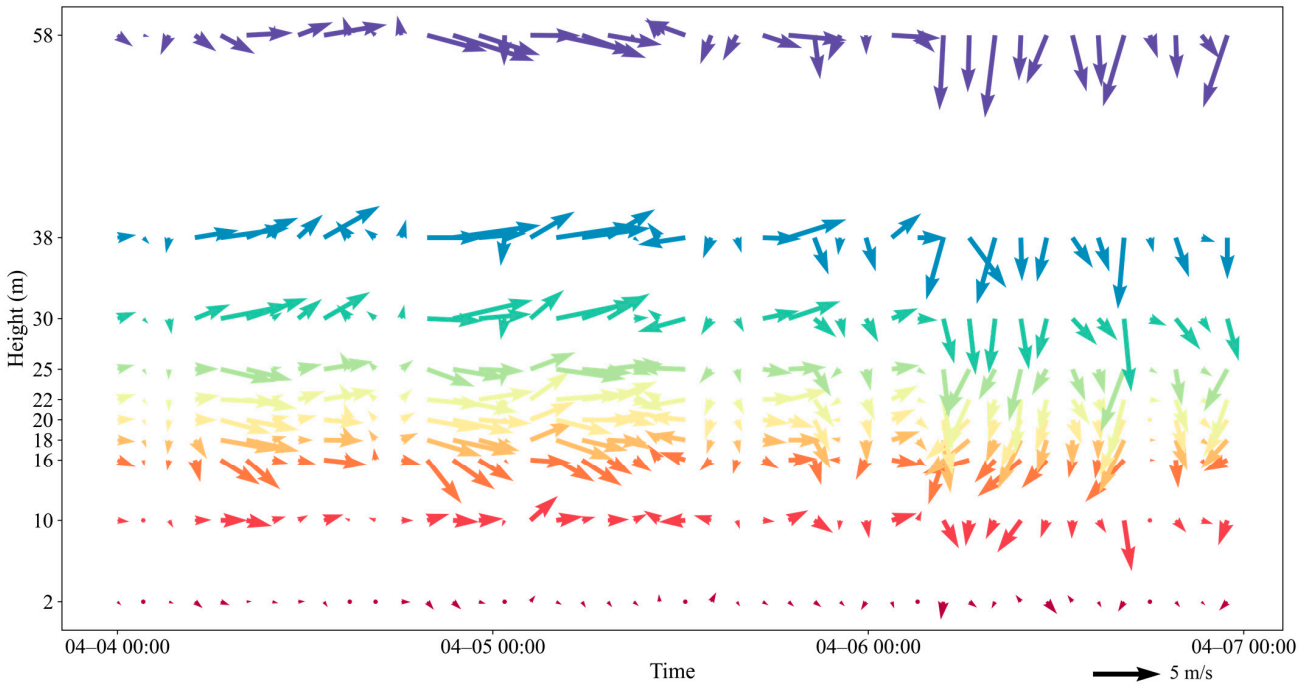


Figure 8. Temporal Variation of Wind Observed by the Boundary Layer Low-Level Wind Tower.

During the day, the wind direction tends to be more consistent across different altitude levels due to enhanced turbulence mixing, which leads to a unification of wind directions throughout the boundary layer. In contrast, at night, especially in the lower layers, wind direction varies frequently, showing multi-directionality. This reflects the instability of wind direction within the boundary layer, which is strongly influenced by local terrain, radiative cooling, and the formation of inversion layers. At lower levels (2 m and 10 m), wind speeds are lower, and wind directions fluctuate significantly due to the influence of surface roughness and complex terrain. This suggests that wind at these levels is more susceptible

to local topographic and thermal effects. As the altitude increases to the middle levels (16 m and 30 m), wind speed begins to increase, and wind direction becomes more stable compared to lower levels but still shows some variability. This indicates a transitional zone where both local influences and larger-scale dynamics are at play. At the higher levels (38 m and 58 m), wind speeds reach their maximum and wind direction becomes more consistent. This suggests that at these levels, the influence of local terrain diminishes, and the wind is primarily controlled by larger-scale atmospheric processes. This pattern highlights that lower-level winds are more affected by surface conditions, resulting in greater variability in both wind speed and direction, while airflow at higher levels is more stable, with stronger wind speeds and more uniform wind directions.

Overall, the variation in wind speed and direction within the boundary layer reflects the combined impact of surface heating and cooling, local topography, and atmospheric boundary layer processes. Since lower-level air is closer to the surface, it is more vulnerable to temperature changes and topographic influences, resulting in lower wind speeds and more variable wind directions. In contrast, higher-level air is less affected by these surface influences, leading to higher wind speeds and more stable wind directions.

3.2. The ABLH Characteristics

3.2.1. Temporal Distribution Characteristics of ABLH

Figure 9 shows the diurnal variation of boundary layer height as observed by UAVs and simulated by the WRF model. It can be seen that the trends are generally consistent between the two, reflecting significant changes in boundary layer height over time. The boundary layer height begins to increase in the early morning, typically rising gradually after 08:00, reaching its peak around noon, with a maximum height of up to 900 m. This phenomenon is primarily due to solar radiation heating the surface during the day, which raises ground temperatures, enhances thermal convection, and leads to the thickening of the boundary layer, forming a substantial mixed layer. As solar radiation decreases, the boundary layer height starts to decline. At night, radiative cooling causes the air stratification to stabilize, significantly reducing turbulence activity and resulting in a notable decrease in boundary layer height, typically only reaching 100–200 m, forming a thin stable layer. This diurnal variation pattern indicates that the development of the boundary layer during the day is dominated by solar radiation, while at night, surface cooling and stable stratification cause the boundary layer to contract.

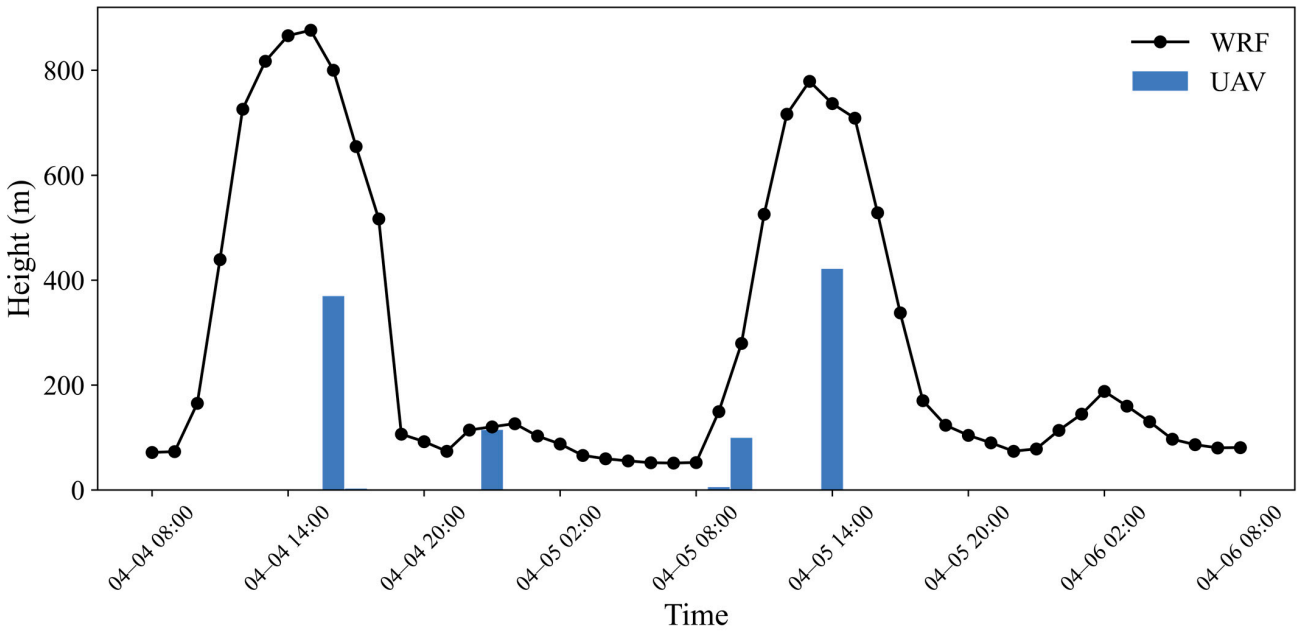


Figure 9. Comparison of Boundary Layer Heights from UAV Observations and WRF Simulations.

3.2.2. Spatial Distribution Characteristics of ABLH

Figure 10 shows the spatial distribution of ABLH at four different times of the day. At 02:00, the boundary layer height is generally low, with most areas below 300 m, indicating a stable stratification characteristic of nighttime conditions. By 08:00, the boundary layer height has slightly increased, yet remains relatively low, with most areas below 600 m. This suggests limited surface heating and weak turbulence in the early morning. At 14:00, the boundary layer height rises significantly, reaching between 600 and 1200 m, with some localized areas even higher. This increase is attributed to strong daytime heating and enhanced convective activity, which thickens the boundary layer. By 20:00, the boundary layer height decreases again, dropping back to around 300 m, reflecting the cooling effect as solar radiation diminishes.

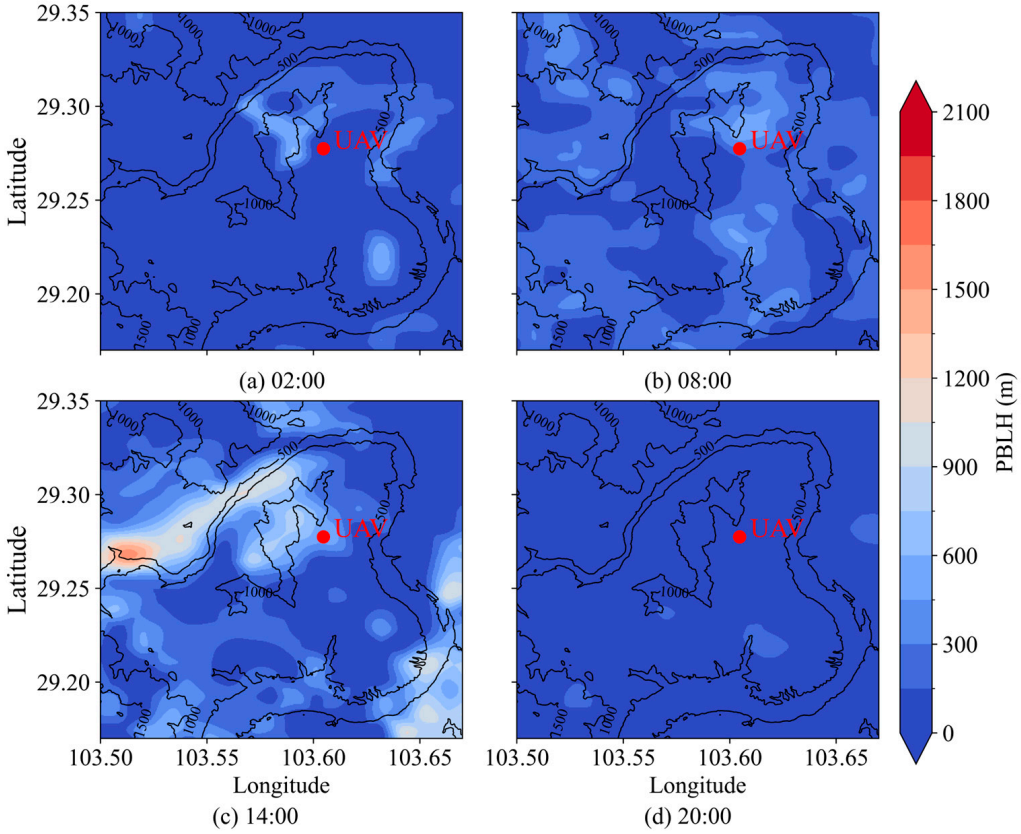


Figure 10. Spatial distribution of ABLH at different times based on daily averages from WRF simulations. (The solid lines represent the topographic contour lines at intervals of 500 m. The red dot indicates the location of the UAV observation station.).

These results are consistent with the previous analysis, showing that the boundary layer height increases significantly during the day, particularly in the afternoon, mainly due to the development of turbulence and the mixed layer triggered by surface solar heating, making the boundary layer thicker. At night, as solar radiation weakens and surface cooling occurs, the boundary layer becomes more stable, and its height decreases significantly. This stable boundary layer limits vertical turbulence mixing and reduces the exchange of heat and momentum in the near-surface atmospheric layer.

It is evident that changes in boundary layer height are directly influenced by surface heating and cooling processes, playing a crucial role in controlling the exchange of matter and energy in the atmosphere.

4. Discussions

This study provides crucial insights into the characteristics of the atmospheric boundary layer (ABL) at Mount Si'e, located on the southeastern edge of the Tibetan Plateau. During the observation period, the boundary layer height (ABLH) can reach up to 900 m during the day and drop to between 100 and 200 m at night. This diurnal variation emphasizes the strong influence of solar radiation and surface temperature changes on boundary layer dynamics, reinforcing previous findings [1,2]. This observation is consistent with the findings of Wen Xiaohang et al., who reported that ABLH is generally lower in forested areas [22].

The significant increase in ABLH during the day is primarily attributed to enhanced thermal convection resulting from solar heating of the surface. This aligns with studies conducted in other mountainous regions, where daytime surface heating plays a critical role in boundary layer formation. At night, surface radiative cooling leads to a decrease in ABLH, creating a stable nocturnal layer. Additionally, the unique microclimatic effects introduced by the complex topography and forest coverage in the Mount Si'e area notably influence wind speed and direction. Higher wind speeds from the southwest may arise from topographical wind corridor effects, while forest coverage increases surface roughness, thereby reducing near-surface wind speeds. The diurnal changes in wind speed and direction further highlight the profound impact of surface heating and cooling. During the day, enhanced solar radiation boosts turbulent mixing, resulting in increased wind speeds, particularly in the lower layers. Conversely, nighttime cooling stabilizes the boundary layer and reduces wind speeds. This pattern is consistent with observations in other mountainous regions, where complex terrain significantly affects the vertical distribution of wind speed and direction compared to flat areas [32].

Discrepancies between our findings and previous research warrant further exploration. While previous studies have documented various ABL heights across the Tibetan Plateau, the specific mechanisms leading to the pronounced nighttime reduction in ABLH observed in this study remain unclear. Factors such as radiative cooling and atmospheric stability at night may contribute to this phenomenon, as highlighted in studies of land-atmosphere interactions [8]. Clarifying these mechanisms is essential for a deeper understanding of ABL processes in this region.

Moreover, unexpected results, such as the pronounced differences in diurnal wind speeds, illustrate the inherent complexity of boundary layer dynamics. Our findings indicate that daytime wind speeds range from 4 to 8 m/s, decreasing to 2 to 4 m per second at night. This diurnal pattern may reflect the typical thermal stratification effects in mountainous regions, where daytime heating enhances turbulence and mixing, while nighttime cooling stabilizes the atmosphere.

However, limitations in this study primarily stem from the temporal and spatial extent of the observations. Although UAV technology allows for high-resolution data collection, the need for manual operation restricts the number and duration of observation points, potentially missing the full variability present across the Tibetan Plateau. Previous research has noted significant variations in boundary layer characteristics over short distances due to topographical changes [7,29]. Future research should consider extending observation durations and expanding the network to encompass a broader range of elevations and geographical features, enhancing the representativeness of the findings. Exploring the potential impacts of climate change on boundary layer characteristics should also be prioritized. Given the region's sensitivity to climatic variations, understanding how ABL dynamics may shift in response to global warming could have significant implications for regional hydrology, ecosystem stability, and climate feedback mechanisms.

5. Conclusions

The boundary layer plays a critical role in the atmosphere for the transport of momentum, heat, and matter. The variations of meteorological elements within it contain important information about the occurrence and development of convection. This study

provides a detailed analysis of the April boundary layer characteristics in the Mount Si'e region of Sichuan, based on data from rotary-wing UAVs, lidar, and WRF simulations. Compared to traditional observation methods, UAVs offer high temporal resolution boundary layer profile data, facilitating a more in-depth analysis of the dynamic and thermal conditions of the boundary layer. The main findings of this study are as follows:

1. During April in the Mount Si'e region, the boundary layer height shows a notable diurnal variation. Daytime heating drives intense thermal convection, raising the boundary layer to a peak of around 900 m, generally ranging between 600 to 1200 m, with localized areas occasionally exceeding this. At night, radiative cooling causes the boundary layer to drop to 100–200 m, forming a stable layer, typically staying below 300 m.
2. Daytime temperatures reach up to 18°C, while humidity drops to around 35%, reflecting active vertical mixing. At night, temperatures drop significantly, reducing the near-surface temperature gradient, while humidity rises above 50%.
3. Prevailing winds in the Mount Si'e region mainly come from the south-southwest, south, and southwest. Daytime wind speeds range from 4 to 8 m/s, occasionally exceeding 8 m/s due to enhanced turbulence. At night, wind speeds decrease to 2–4 m/s, influenced by local topography, vegetation, and stable atmospheric conditions.

In conclusion, this study, through the combined use of rotary-wing UAVs, high-resolution soundings, and the WRF model, reveals the typical April boundary layer characteristics in the Mount Si'e region of Sichuan, providing valuable scientific data for understanding boundary layer processes in the eastern part of the plateau. The findings not only offer important insights for improving boundary layer parameterization schemes and numerical weather prediction models but also lay the foundation for further research into the complex dynamic and thermal processes within the boundary layer. This study demonstrates the potential of UAV observations in enhancing boundary layer parameterization schemes. High-resolution UAV data on boundary layer height, wind speed, and thermal conditions can be used to calibrate and validate existing parameterization schemes, particularly in complex terrain and local thermal environments, improving the accuracy of turbulent mixing and thermal exchange modeling. Furthermore, integrating UAV data into numerical weather prediction models via data assimilation can significantly improve the representation of boundary layer structure in models, thus enhancing forecasting accuracy for local convective weather and wind field variations. Future work will continue to explore the potential application of UAV data in numerical model data assimilation to improve the forecasting capabilities for local convective weather.

Author Contributions: Conceptualization, J.D., methodology and writing, X.X. and X.W. All authors have read and agreed to the published version of the manuscript.

Funding: The Second Tibetan Plateau Scientific Expedition and Research Program (STEP) (grant number 2019QZKK010304). The National Natural Science Foundation of China (grant number 41975096) and the Technological Innovation Capacity Enhancement Program of the Chengdu University of Information Technology (grant number KYQN202203) provided financial support for this study.

Data Availability Statement: The original contributions presented in the study are included in the article, further inquiries can be directed to the corresponding author.

Conflicts of Interest: The authors declare no conflicts of interest.

References

1. *An Introduction to Boundary Layer Meteorology*; Stull, R.B. (Ed.) Springer: Dordrecht, The Netherlands, 1988; ISBN 978-90-277-2769-5.
2. Su, Y.; Lü, S.; Fan, G. The Characteristics Analysis on the Summer Atmospheric Boundary Layer Height and Surface Heat Fluxes over the Qinghai-Tibetan Plateau. *Plateau Meteorol.* **2018**, *37*, 1470–1485.
3. Li, Y.; Hu, Z.; Zhao, H. Overview on the Characteristic of Boundary Layer Structure in Tibetan Plateau. *Plateau Mt. Meteorol. Res.* **2012**, *32*, 91–96.

4. Baklanov, A.A.; Grisogono, B.; Bornstein, R.; Mahrt, L.; Zilitinkevich, S.S.; Taylor, P.; Larsen, S.E.; Rotach, M.W.; Fernando, H.J.S. The Nature, Theory, and Modeling of Atmospheric Planetary Boundary Layers. *Bull. Amer. Meteor. Soc.* **2011**, *92*, 123–128. [CrossRef]
5. Zhang, Q.; Zhang, J.; Qiao, J.; Wang, S. Relationship of Atmospheric Boundary Layer Depth with Thermodynamic Processes at the Land Surface in Arid Regions of China. *Sci. China Earth Sci.* **2011**, *54*, 1586–1594. [CrossRef]
6. Zhao, M. A Review of the Research on the Effects of Boundary Layer and Land Surface Process on Heavy Rain in China. *Torrential Rain Disasters* **2008**, *2*, 186–190.
7. Ma, Y.; Hu, Z.; Wang, B.; Ma, W.; Chen, X.; Han, C.; Li, M.; Zhong, L.; Gu, L.; Sun, F.; et al. The Review of the Observation Experiments on Land-Atmosphere Interaction Progress on the Qinghai-Xizang(Tibetan)Plateau. *Plateau Meteorol.* **2021**, *40*, 1241–1262.
8. Fu, W.; Li, M.; Yin, S.; Lü, Z.; Wang, L.; Shu, L. Study on the Atmospheric Boundary Layer Structure of the Qinghai-Xizang Plateau under the South Branch of the Westerly Wind and the Plateau Monsoon Circulation Field. *Plateau Meteorol.* **2022**, *41*, 190–203.
9. Song, X.; Zhang, H.; Liu, X.; Fan, S.; Liu, H.; Hu, F.; Li, S.; Zhou, M.; Bian, L.; Xu, X. Determination of Atmospheric Boundary Layer Height in Unstable Conditions over the Middle Tibetan Plateau. *Acta Sci. Nat. Univ. Pekin.* **2006**, *42*, 328–333.
10. Jiang, X.; Li, Y.; He, G. The Climatic Characteristics Analysis of Radiosonde Data over East Part of Tibetan Plateau. *Plateau Mt. Meteorol. Res.* **2008**, *28*, 1–9.
11. Ye, D. *Meteorology of the Tibetan Plateau*, 1st ed.; Science Press: Beijing, China, 1979.
12. Xu, X.; Zhou, M.; Chen, J.; Bian, L.; Zhang, G.; Liu, H.; Li, S.; Zhang, H.; Zhao, J.; Suolang, D.; et al. Comprehensive Physical Representation of the Dynamic and Thermal Structure of the Land-Atmosphere Processes on the Tibetan Plateau. *Sci. Sin.* **2001**, *31*, 428–441.
13. Li, M.; Dai, Y.; Ma, Y.; Zhong, L.; Lü, S. Analysis on Structure of Atmospheric Boundary Layer and Energy Exchange of Surface Layer over Mount Qomolangma Region. *Plateau Meteorol.* **2006**, *25*, 807–813.
14. Chen, X.; Añel, J.A.; Su, Z.; De La Torre, L.; Kelder, H.; Van Peet, J.; Ma, Y. The Deep Atmospheric Boundary Layer and Its Significance to the Stratosphere and Troposphere Exchange over the Tibetan Plateau. *PLoS ONE* **2013**, *8*, e56909. [CrossRef] [PubMed]
15. Gu, L.; Yao, J.; Hu, Z.; Ma, Y.; Sun, F.; Yu, H.; Wang, S.; Yang, Y.; Guo, R.; Qin, Y. Characteristics of the Atmospheric Boundary Layer's Structure and Heating (Cooling) Rate in Summer over the Northern Tibetan Plateau. *Atmos. Res.* **2022**, *269*, 106045. [CrossRef]
16. Yang, K.; Koike, T.; Fujii, H.; Tamura, T.; Xu, X.; Bian, L.; Zhou, M. The Daytime Evolution of the Atmospheric Boundary Layer and Convection over the Tibetan Plateau: Observations and Simulations. *J. Meteorol. Soc. Jpn. Ser. II* **2004**, *82*, 1777–1792. [CrossRef]
17. Li, F.; Zou, H.; Zhou, L.; Ma, S.; Li, P.; Zhu, J.; Zhang, Y. Study of Boundary Layer Parameterization Schemes'Applicability of WRF Model over Complex Underlying Surfaces in Southeast Tibet. *Plateau Meteorol.* **2017**, *36*, 340–357.
18. Che, J.; Zhao, P. Characteristics of the Summer Atmospheric Boundary Layer Height over the Tibetan Plateau and Influential Factors. *Atmos. Chem. Phys.* **2021**, *21*, 5253–5268. [CrossRef]
19. Zuo, H.; Hu, Y.; Li, D.; Lü, S.; Ma, Y. Seasonal Transition and Its Boundary Layer Characteristics in Anduo Area of Tibetan Plateau. *Prog. Nat. Sci.* **2005**, *15*, 239–245.
20. Li, M.; Ma, Y.; Ma, W.; Ishikawa, H.; Sun, F.; Shin-Ya, O. Structural Difference of Atmospheric Boundary Layer between Dry and Rainy Seasons over the Central Tibetan Plateau. *J. Glaciol. Geocryol.* **2011**, *33*, 72–79.
21. Zhou, W.; Yang, S.; Jiang, X.; Guo, Q. Study of the Atmospheric Boundary Layer Height over the Tibetan Plateau Using COSMIC Radio Occultation Data. *Acta Meteorol. Sin.* **2018**, *76*, 117–133.
22. Wen, X.; Ma, J.; Chen, M. Analysis of Atmospheric Boundary Layer Characteristics on Different Underlying Surfaces of the Eastern Tibetan Plateau in Summer. *Remote Sens.* **2024**, *16*, 1645. [CrossRef]
23. Li, Y.; Li, Y.; Zhao, X. The Comparison and Analysis of ABL observational data between the East of Tibetan Plateau and Chengdu Plain (I). *Plateau Mt. Meteorol. Res.* **2008**, *28*, 30–35.
24. Lo, J.C.-F.; Yang, Z.-L.; Pielke, R.A., Sr. Assessment of Three Dynamical Climate Downscaling Methods Using the Weather Research and Forecasting (WRF) Model. *J. Geophys. Res.* **2008**, *113*, 2007JD009216. [CrossRef]
25. Seibert, P.; Beyrich, F.; Gryning, S.-E.; Joffre, S.; Rasmussen, A.; Tercier, P. Review and Intercomparison of Operational Methods for the Determination of the Mixing Height. *Atmos. Environ.* **2000**, *34*, 1001–1027. [CrossRef]
26. Yang, F.Y. Comparison of Determination Methods and Characteristics of Boundary Layer Height in Semi-Arid Area. PhD Thesis, Lanzhou University, Lanzhou, China, 2018.
27. Garratt, J.R. The Atmospheric Boundary Layer. *Earth-Sci. Rev.* **1994**, *37*, 89–134. [CrossRef]
28. Culf, A.D.; Fisch, G.; Malhi, Y.; Nobre, C.A. The Influence of the Atmospheric Boundary Layer on Carbon Dioxide Concentrations over a Tropical Forest. *Agric. For. Meteorol.* **1997**, *85*, 149–158. [CrossRef]
29. Mahrt, L. Stratified Atmospheric Boundary Layers. *Bound.-Layer Meteorol.* **1999**, *90*, 375–396. [CrossRef]
30. He, Y.; Zhu, X.; Sheng, Z.; He, M. Identification of Stratospheric Disturbance Information in China Based on the Round-Trip Intelligent Sounding System. *Atmos. Chem. Phys.* **2024**, *24*, 3839–3856. [CrossRef]

31. Ayet, A.; Chapron, B. The Dynamical Coupling of Wind-Waves and Atmospheric Turbulence: A Review of Theoretical and Phenomenological Models. *Bound.-Layer Meteorol.* **2022**, *183*, 1–33. [CrossRef]
32. Gohm, A.; Harnisch, F.; Vergeiner, J.; Obleitner, F.; Schnitzhofer, R.; Hansel, A.; Fix, A.; Neininger, B.; Emeis, S.; Schäfer, K. Air Pollution Transport in an Alpine Valley: Results from Airborne and Ground-Based Observations. *Bound.-Layer Meteorol.* **2009**, *131*, 441–463. [CrossRef]

Disclaimer/Publisher's Note: The statements, opinions and data contained in all publications are solely those of the individual author(s) and contributor(s) and not of MDPI and/or the editor(s). MDPI and/or the editor(s) disclaim responsibility for any injury to people or property resulting from any ideas, methods, instructions or products referred to in the content.